Simulation-guided PGD-Stereocorrelation for hybrid testing

Xuyang Chang, Bastien Bodnar, Jan Grashorn, François Hild, Fabrice Gatuingt, Stéphane Roux

Simulation-guided PGD-Stereocorrelation for hybrid testing

Xuyang Chang[1,2*†], Bastien Bodnar[3,2†], Jan Grashorn[4,5], François Hild[2], Fabrice Gatuingt[2] and Stéphane Roux[2]

[1]University of Science and Technology in Beijing, 30, Xueyuan Road, Haidian District, Beijing, 100030, China.
[2]Université Paris-Saclay, CentraleSupélec, ENS Paris-Saclay, CNRS, LMPS – Laboratoire de Mécanique Paris-Saclay, 4 avenue des Sciences, 91190 Gif-sur-Yvette, France.
[3]Conservatoire National des Arts et Métiers, Laboratoire de Mécanique des Structures et des Systèmes Couplés 292 rue Saint-Martin, 75141 Paris Cedex 03, France.
[4]Institute for Risk and Reliability, Leibniz University Hannover, Callinstr. 37, 30167 Hannover, Germany.
[5]International Research Training Group 2657, Leibniz University Hannover, Appelstr. 11a, 30167 Hannover, Germany.

*Corresponding author(s). E-mail(s): xuyang.chang@ustb.edu.cn;
†These authors contributed equally to this work.

Abstract

Hybrid testing aims to evaluate the dynamics of a large scale structure from which an isolated part is experimentally tested, while the rest is simulated in the control loop for imposing earthquake-induced motions at boundaries. One of these tests, led in real-time on a three-story reinforced concrete structure to quantify damage due to successive multiaxial seismic loadings, and focusing experimentally on a single column, is considered in this study.

Stereocorrelation (SC) using high speed cameras is an appealing technique to further analyze such tests, providing 3D surface displacement fields and damage indications. Assuming a spacetime separation of the

kinematics and constructing a tailored temporal basis, Proper Generalized Decomposition SC (PGD-SC) is well-suited to handle long image series efficiently. Furthermore, it aligns perfectly with the philosophy of model (hyper-)reduction on the simulation side as needed for real-time control.

The present study explores the potential of using temporal modes extracted from both existing simulations and image series for SC analyses. It is shown that the simulation-guided PGD-SC outperforms the classical PGD-SC in terms of computation time with a minimal implementation effort. The kinematic measurements also highlight the direction in which the numerical model should be refined to better account for the observed non-linearities. The perspective of using such simulation-guided PGD-SC into hybrid testing protocols (including pseudo-dynamic experiments) appears credible.

Keywords: Proper Generalized Decomposition, Stereocorrelation, Real-Time Hybrid Testing

1 Introduction

The advent of high-speed and ultra-high-speed cameras opens new venues for Stereo-Correlation (SC) in dynamic testing [1–5]. When temporal series of images (or movies) are acquired to analyze dynamic tests, a spacetime formulation of SC [6, 7] (*i.e.,* 3D displacements of the sample surface, and 1D in time) allows higher temporal resolutions of kinematic fields to be reached at the cost of handling the acquired big data set.

In the early study of SC, clouds of scattered 3D physical points [8, 9] are often used to describe the shape and the kinematics of investigated specimen surfaces, termed as "local approach." Later on, with the rapid increase in computational power, the "global approach" was conceptualized. The idea is to use fewer degrees of freedom (*e.g.,* finite-element facets ([10–13] or free-form (isogeometric) surfaces [14–16]) to describe the initial shape and its deformation without compromising its accuracy. Thanks to the reduced number of unknowns and the improved conditioning of the Hessian matrices, the global framework of SC displays lower displacement uncertainties [17, 18]. More importantly, the global SC framework allows for an easy handling of heavy image stacks by introducing a set of temporal shape functions (*i.e.,* with so-called "spacetime approach"). The work of Ref. [19] proves that when using any set of orthonormal temporal shape functions, solving the spacetime SC problem is equivalent to solving each modal problem independently with the exact same memory load as for instantaneous schemes.

Selecting an orthonormal temporal basis in the spacetime formulations of SC is relatively unrestricted, and one can freely construct the temporal basis based on prior knowledge (*e.g.,* force history [19], numerical simulations). Alternatively, the temporal shape functions can be equally derived

from error estimates (*i.e.,* gray-level residual or spacetime gradient of the SC cost function) and progressively updated on the fly. The latter approach is called "Proper Generalized Decomposition" Stereocorrelation (PGD-SC) [6, 7]. In these previous studies, the spacetime SC has already proven its superior computation efficiency and robustness compared to instantaneous SC.

Until now, in spacetime SC, the use of these two methods to construct temporal bases was separate. However, using simulation results to guide PGD-SC computations, and combining information from prior knowledge and error estimate altogether is extremely appealing for reasons summarized below:
– As numerical simulations handle an entire specimen, they are exhaustive in their account of the designed experimental test. The information retrieved from numerical simulations can be seen as an "educated" guess to guide the spacetime approach, especially when large displacements are observed.
– The imperfections of the numerical model due to defects introduced at any stage (including the experimental setup) or the departure of the model from the specimen behavior due to its evolution during the test makes it almost impossible to perfectly match simulations with experimental results. In practice, the temporal shape functions should thus be completed by exploring the rich information buried in the error estimates. The temporal shape functions may be updated through a progressive enrichment procedure [7], thereby ensuring the final registration quality.

Hardware-in-the-loop protocols could advantageously benefit from PGD-SC to monitor experiments in real-time as they already use a computational environment from which *prior* temporal modes can be built. This environment includes civil engineering hybrid tests, which consist in using a numerical model that is virtually connected to the physical specimen (*e.g.,* beam, column, or frame) to account for the dynamics of the untested components (*i.e.,* upper stories, or adjacent frames) [20]. The *online* processing of the data recorded for DIC purposes consequently includes many possibilities:
– First, when equiped with high-speed cameras, PGD-SC allows for full-field non-contact measurements of the kinematics in space and time domains. This route possibly replaces displacement sensors, which are not easy to install on tall specimens and may be subjected to sliding or shocks at contact areas. More importantly, the finite-element representation of the measured displacement fields provides a seamless dialogue between tests and simulations, thus enabling for extremely discriminative cross-validations.
– Second, thanks to the underlying brightness conservation between images registered in the reference and deformed configurations, the gray-level residuals highlight faithfully the detailed evolution of crack growth (including progressive crack opening/closure phenomena inside the region of interest, even at a small spatial amplitude) [3, 5]. These local nonlinearities are rather difficult to predict from numerical simulations. In this regard, SC provides a potential enrichment of the constitutive models (*i.e.,* adding damaged-related nonlinearities into current simplified models), but also allows for an *online* quantification of the crack lengths, making it possible to adjust the loading rate to better

capture damage growth.
– Last, the measured kinematic data can be directly used in the framework of DIC-based Finite-Element Model Updating [21] to calibrate constitutive models, thereby improving hybrid tests by updating the behavior of the computational environment with respect to the response of the specimen.

As a first step toward using PGD-SC in hybrid tests, it is proposed to *post-process* an innovative test case to assess the feasibility of such an approach. The chosen proof of concept consists in a real-time hybrid test (RTHT) (*i.e.,* partly experimental and partly simulated) on a reinforced concrete column (RCC) subjected to a bidirectional loading [20]. The RCC is virtually connected to a numerical model of an irregular three-story building to account for real-world (*i.e.,* in-situ) conditions. The structure is subjected to an earthquake of strong intensity and is modeled using a quasi-brittle damage law for concrete [22] with a bilinear elastoplastic law for steel. Using a hybrid testing protocol, loading paths faithfully representing the dynamic response of the entire structure are achieved despite only testing a substructure of it experimentally. A hyper-reduction strategy is additionally used to decrease the computational cost of the finite element analysis and to run real-time simulations [23–26]. Recent works demonstrated that hyper-reduced order models (HROMs) are able to correctly describe nonlinear dissipative mechanisms (*e.g.,* damage, frictional sliding, and stiffness recovery) on simulated reinforced concrete structures under cyclic loadings [27, 28].

To the best of the authors' knowledge, if some researchers already used DIC during pseudo-dynamic (PsD) hybrid tests (*i.e.,* on which the specimen is loaded in deferred time) [29, 30], the applicability of stereocorrelation to RTHTs has never been investigated, nor have temporal modes been extracted from the computational environment (*i.e.,* simulated parts of the structure) to guide spacetime kinematic registrations. The paper is organized as follows. Section 2 presents the hybrid testing setup and the stereovision system. Section 3 introduces the implementation of the simulation-guided PGD-SC framework. Section 4 discusses the kinematic results. Conclusions and perspectives are drawn in Section 5. Appendix A provides details about the (physical) RCC, the virtual frame structure and material properties. Appendix B summarizes the hardware and software parameters of the stereovision system.

2 Experimental setup

2.1 Real-Time Hybrid Testing Protocol

The experiment exploited in the present study aims at studying seismic damage of a large three-story building. A frame structure made of reinforced concrete is subjected repeatedly to a seismic load to investigate the effect of accumulated damage on its main column, which significantly contributes to the strength of the frame. To address this analysis experimentally, a hybrid testing protocol [31–34] coupled with a substructuring strategy [35–40] is implemented. The spirit is to concentrate the experimental part only on one (critical) part

of the building, namely, a reinforced concrete column (RCC), while the rest of the structure is simulated to compute real-time commands for the servohydraulic systems (as illustrated in Figure 1). Force feedbacks are then measured on the physical specimen, on boundaries with the numerical model, to be used as external loads along with the earthquake [41].

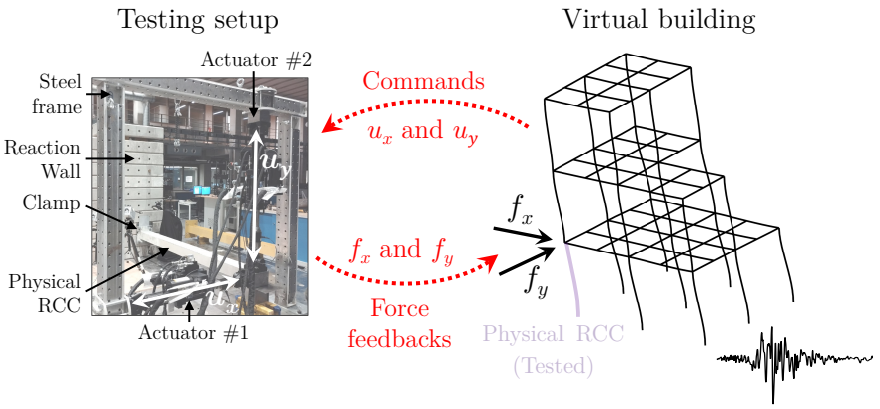

Fig. 1 Bidirectional real-time hybrid testing procedure. (left) Physical reinforced concrete column. (right) Virtual reinforced concrete frame structure.

The choice has been made to introduce a hard constraint on the setup as the specimen is loaded dynamically [42, 43], which is not strictly necessary for the case under study (*i.e.,* the RCC is not rate-dependent) but investigated as a first step toward more complex experiments [44–49]. The main challenge is thus to simulate the frame (*i.e.,* complementary part of the RCC) in real-time although it is subjected to significant nonlinearities (due to damage and plasticity of the reinforcements). To meet this objective, a hyper-reduction strategy is followed [23–26].

2.1.1 Reinforced Concrete Column

The main features of the physical RCC are briefly given hereafter, and Appendix A provides a more detailed description. The specimen size is 15×22 cm (cross-section) and 3 m in length. It is made of concrete of class C 30/37, inside which steel reinforcements settle (detailed in Appendix A). One of its boundary is clamped to a reaction wall at one end, and the other is virtually pin-connected at its top to the numerical model (Figure 1). As the testing platform is not large enough to add a third actuator along the z-axis, the vertical force entries are numerically computed to further decrease the complexity of the setup. Despite not blocking rotations or prescribing axial loads, the physical/virtual connection is still relevant as it succeeds in prescribing earthquake-induced inter-story drifts to the RCC, which is the main benefit of hybrid testing for the case under study.

2.1.2 Virtual substructure

The three-story reinforced concrete frame building (Figure 2) is used as a virtual substructure, whose geometrical irregularities in plane and height generate torsion at floor level. A more detailed description is given in Appendix A.

The discretized finite element model comprises nonlinear multifiber beams accounting for damage and plasticity [50]. This semi-global model uses beam kinematics to evaluate local strains over the areas of the cross-sections, on which integration points (or fibers) are set to locally update concrete and steel properties. The beam and the column elements are 50 cm and 25 cm long, respectively, while cross-sections are discretized into 3×5 surface elements for the beams and 5×5 surface elements for the columns. Four integration points per surface element model concrete, and one per longitudinal reinforcement accounts for steel.

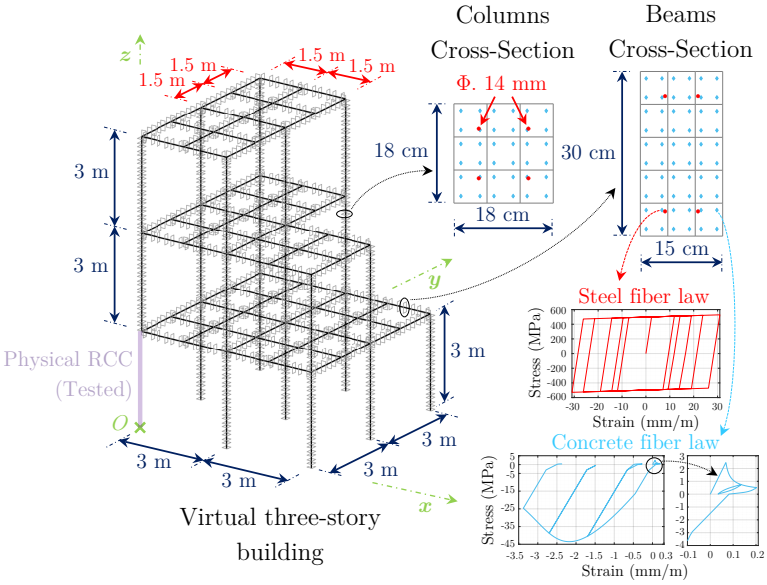

Fig. 2 Virtual three-story structure. (left) Discretized multifiber beam model with cross-sections at Gauss points (upper right) mesh of the cross-sections (lower right) steel and concrete constitutive laws.

All in all, the virtual substructure is modeled with 499 nodes linked by 546 multi-fiber beams. The matrix system to solve includes 2946 degrees of freedom, while material properties are updated on 52,848 concrete and 4,368 steel fibers distributed on 1092 cross-sections localized at the Gauss points of the beam support. A quasi-brittle damage law with frictional sliding and stiffness recovery models concrete [22], while a bilinear elastoplastic law with kinematic hardening is used for steel. The parameters of the constitutive laws are summarized in Appendix A. To account for energy dissipation at column-beam

connections and also to stabilize the dynamic analysis, a constant Rayleigh viscous damping is added to the model [51].

2.1.3 Loading scenario

The earthquake shown in Figure 3 models the seismic hazard. Its peak ground acceleration is 0.36 g, which is high enough to activate damage and plasticity in the model. The signal is weighted by 1.00 along the x-axis, 0.65 along the y-axis, and 0.30 along the z-axis to generate a three-component earthquake that activates torsion at floor level.

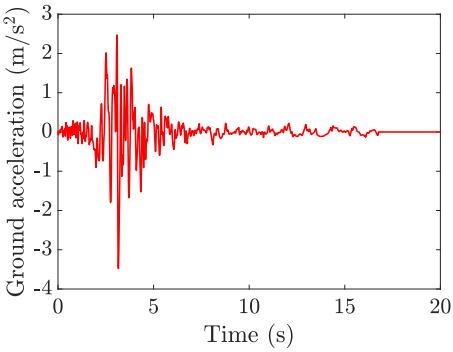

Fig. 3 Ground acceleration of the earthquake on runs #1, #2, and #3.

This loading is repeatedly used three times during the test, each one being referred to as a "run", to evaluate how pre-existing damage may grow inter-story drifts. Because internal variables are not reset from one run to the next, commands depend on the loading history of both physical RCC and virtual building, which includes the dead and live loads (*i.e.,* quasi-statically applied to initialize the dynamic analysis), as well as the seismic loads from the previous runs.

The finite element analysis is run in a MATLAB® kernel implemented in a host computer. Commands are updated by solving the matrix system every 10 ms. A multi-rate hybrid testing strategy [52, 53] then continuously interpolates the displacements to control the actuators at a sampling rate of 1024 Hz. In addition, an α-operator splitting (α-OS) time integration method allows simulating the nonlinear model without iterating nor being dependent on its largest natural frequency, which is possible with softening mechanisms [41, 54].

2.1.4 Hyper-reduction of the nonlinear model

As the high-dimensional model introduces complex nonlinear phenomena (*i.e.,* damage and plasticity) on a large part of the mesh, it cannot be simulated in real-time. An *a posteriori* hyper-reduction strategy, known as Proper Orthogonal Decomposition (POD) Unassembled Discrete Empirical Interpolation Method (DEIM), is used to approximate its dynamics.

It uses POD to identify displacement and force bases from training datasets [55]. Modes are then selected to build a displacement basis that handles nonlinearities when reducing the size of the matrix system [56], along with an interpolation operator to approximate the force entries only using quantities computed at specific parts of the mesh (*e.g.,* on a reduced subset of elements, or at Gauss points), all belonging to a reduced integration domain (RID) [23, 24, 27, 28]. The computational cost of the HROM is minimized to ensure that its error with the full order model does not exceed 0.3% at run #1. Optimal settings are found using 19 modes for the displacement basis and a subset of 64 Gauss points as a reference to approximate the force entries, which is only 6% of the mesh.

Figure 4 displays the shapes of POD modes #1, #2, and #3, provides an estimate of their activating frequency based on the Rayleigh-Ritz method [57], and locates the Gauss points of the RID on the mesh. All modes mainly contribute to floor-level bending and torsion, with an additional dependence of POD mode #2 to the vertical loads. Figure 5 then shows that the dynamic response of the model mainly depends on bending, and that hyper-reduction approximates the commands of both actuators (*i.e.,* U_x, and U_y) with a negligible error.

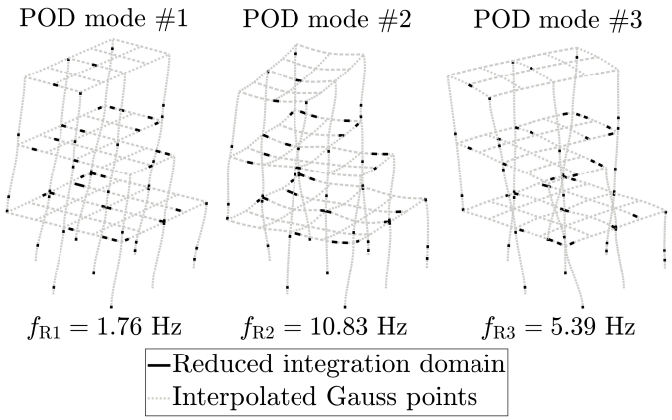

Fig. 4 Hyper-reduced order model. POD modal shapes #1 (left), #2 (middle), and #3 (right) and reduced integration domain on which concrete properties need to be updated (*i.e.,* 64/1092 beam Gauss points, $\approx$ 6 % of the mesh).

Because the full order model is condensed into a 22 DOF matrix system (*i.e.,* with 19 reduced coordinates and the three boundary DOFs coupling the physical and virtual substructures) that only uses 6 % of the mesh, the runtime of the finite element analysis is 31 times faster, which allows commands to be updated in approximately 1 ms per runtime. As the time step is 10 ms, overruns during the test are prevented, allowing other processes (*e.g.,* filtering, feed-forward predictions, delay compensations, or analog/digital conversions) to be executed in parallel to smoothen and synchronize data in real-time.

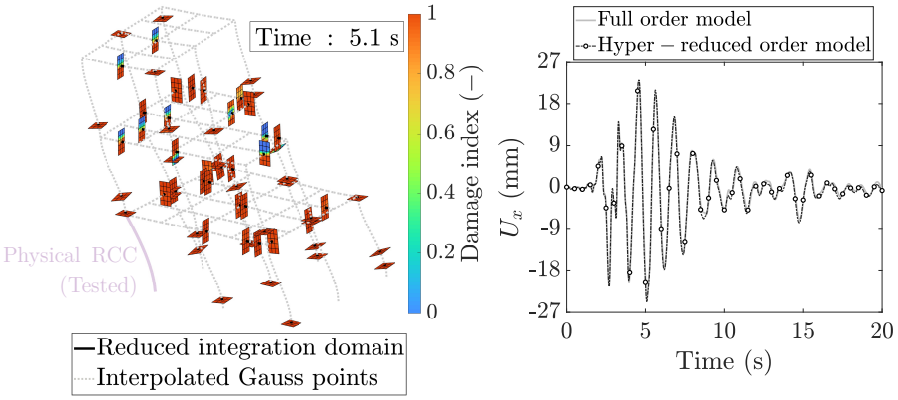

Fig. 5 Dynamic response of the HROM using elastic properties for the specimen. (left) Deformed mesh and damage index on the cross-sections of the RID (amplified 3 times) at time 5.1 s. (right) Comparison of the full and hyper-reduced order models in terms of displacement U_x

2.2 Stereovision system

Figure 6 displays the optical setup. Two high-speed cameras constitute the stereovision system, and a rectangular LED panel provides homogeneous lighting conditions. A black curtain is also set up to provide a uniform background.

The region where the RCC specimen is clamped to the reaction wall, of size $600 \times 230 \times 150$ mm^3, is predicted to be the most critical region for damage development, and is thus chosen as the region of interest (ROI) in the following analyses.

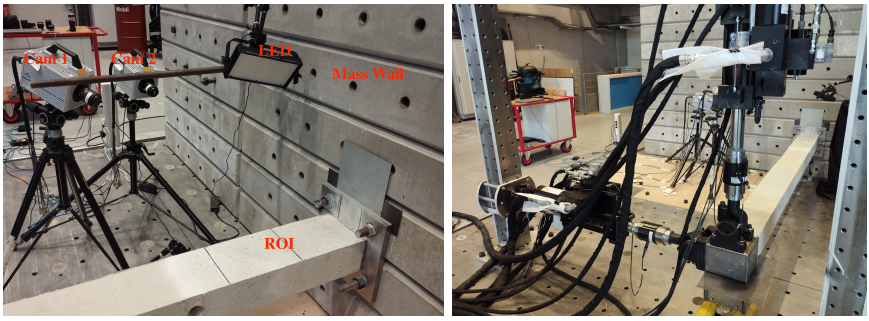

Fig. 6 Experimental setup. (left) Stereovision system. (right) Tested RCC with two actuators

As shown in Figure 7, a multiscale speckle pattern (black dots on the white background) was sprayed onto the observed column faces, with a speckle size ranging from 2 to 16 pixels. For the sake of stereo-calibration, black lines are drawn to outline the ROI. The camera and acquisition parameters are listed in Table 6.

Fig. 7 Reference images captured by the two high-speed cameras. Left and right are respectively cameras 1 and 2

3 Formulation of simulation-guided PGD stereocorrelation (SG-PGD-SC)

3.1 Global Stereocorrelation

In this section, the fundamentals of a global SC algorithm are very briefly recalled. Interested readers are referred to Refs. [4, 15, 58] where instantaneous and spatiotemporal approaches are discussed within a global SC formulation. The analysis focuses on the 3D specimen surfaces. The latter ones are introduced as a surface mesh, defining their shape, and will further be used as support of the displacement field.

The first step, referred to as calibration, allows the homogeneous coordinates of the specimen surfaces $\{\mathbf{X}\} = \{X, Y, Z, 1\}^\top$ to be linked with the homogeneous coordinates of their 2D projections onto the different camera image planes, $\{\mathbf{x}^i\} = \{x^i, y^i, 1\}^\top$ via projections matrices to be calibrated, where i labels the camera [9]. Figure 8 shows the 3D mesh projected in the two camera planes. A very good match is observed.

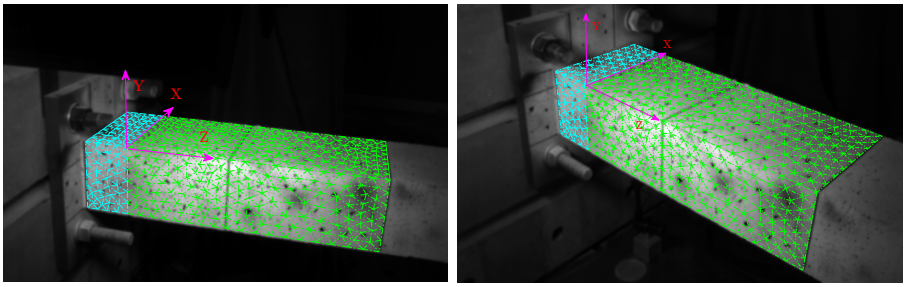

Fig. 8 Projected 3D mesh superimposed with each reference image for cameras 1 (left) and 2 (right). The cyan part of the FE mesh (containing a shadow) was discarded in the registrations.

The specimen-image mappings are then used to transport the speckle pattern as observed in each image onto the 3D surface mesh [4, 15]. To deal with

differences in gray levels of each camera, each speckle image is first normalized to a zero average and unit standard deviation, and their average defines the "intrinsic texture" of the specimen surface, $\widehat{f}(\mathbf{X})$.

The goal of SC is the measurement of the specimen motion from the series of images captured by the cameras. The sought displacement field at time t, $\mathbf{U}(\mathbf{X},t)$, is determined based on the registration of the projection of the deformed specimen speckle with the recorded images. The difference between these two images, referred to as the "residuals", $\rho^i(\mathbf{x}^i,t)$ for camera i, are computed, and the sum of their L2 norm is minimized with respect to the nodal displacements. At convergence, these residuals highlight all the differences that are not accounted for by the measured displacement (*e.g.,* convergence, discretization error, noise, interpolation error, detector artifact, blur [59], brightness and contrast variations [4] or the presence of cracks [3]), and hence reveal extremely precious for interpreting the kinematic analysis. In the following, the gray-level residuals will be shown after normalization by the dynamic range of the corresponding camera. Their norm, either camera-wise or global, are good indicators of the quality of the registration and are also used as a convergence criterion.

The sought displacement field at time t, $\mathbf{U}(\mathbf{X},t)$, is decomposed over the surface mesh

$$\mathbf{U}(\mathbf{X},t) \equiv \sum_{j=1}^{N_s} (a_U)_j(t)\boldsymbol{\Phi}_j(\mathbf{X}) \tag{1}$$

where $\boldsymbol{\Phi}_j$ denotes the j-th (vectorial) spatial shape function, while $\{\boldsymbol{a_U}(t)\}$ collects all nodal displacements at time t. The fineness of the mesh is thus an important tool to tailor the required flexibility of the kinematic description, and to benefit from the spatial regularity provided by the shape functions.

Equation (1) defines the result of an instantaneous analysis. When a time series is to be analyzed, it is natural to exploit the temporal dimension in a similar fashion as the space domain, and introduce a basis of functions, $\psi_m(t)$, with $m = 1, ..., N_t$. Here again, the design of these temporal shape functions allows one to tune flexibility and regularity for a good conditioning of the problem. The displacement field thus writes

$$\mathbf{U}(\mathbf{X},t) = \sum_{j=1}^{N_s}\sum_{m=1}^{N_t} (\alpha_U)_{jm}\boldsymbol{\Phi}_j(\mathbf{X})\psi_m(t) \tag{2}$$

In the spacetime formulation of SC, the nodal displacement vector $\{\boldsymbol{\alpha_U}\}$ is determined through an iterative Gauss-Newton scheme

$$[\mathbf{M}_U]\{\delta\boldsymbol{\alpha_U}\} = \{\mathbf{m_U}\} \tag{3}$$

$$\{\boldsymbol{\alpha}_U^{it+1}\} = \{\boldsymbol{\alpha}_U^{it}\} + \{\delta\boldsymbol{\alpha_U}\} \tag{4}$$

where the spacetime Hessian matrix $[\mathbf{M}_U]$, and spacetime second member $\{\mathbf{m}_U\}$ are expressed as

$$\begin{aligned}(M_U)_{jkmn} &= (H_U)_{jm}(K)_{kn} \\ (m_U)_{jk} &= \int_{t_0}^{t_f} (h_U(t))_j \psi_m(t)\ \mathrm{d}t \end{aligned} \tag{5}$$

with $[\mathbf{H}_U]$ and $[\mathbf{K}]$ the spatial and temporal Hessian matrices, respectively, $\{\mathbf{h_U}(t)\}$ the spatial second member for a given frame t.
Note that the instantaneous formulation simply consists in choosing a single instant indicator, and is thus a particular case of the global spatiotemporal analysis. The problem formulation remains identical, with a cost function to minimize that is the time integral of the residual norm.

An interesting property of the spatio-temporal formulation is that space and time decouple [19]. The global Hessian matrix is the product of a spatial Hessian matrix (identical to the instantaneous problem) and a temporal one, which is nothing but the scalar products of all pairs of temporal shape functions. Thus, choosing an orthonormal basis (or orthogonalizing and normalizing the basis) makes the temporal Hessian equal to the identity matrix. In that case, the full spacetime problem reduces to N_t independent problems whose computation cost is exactly that of an instantaneous problem.

All the SC softward parameters are gathered in Table 7.

3.2 Proper Generalized Decomposition Stereocorrelation

The "PGD" approach consists in updating the orthonormal temporal shape functions on the fly based on the registration residuals [6, 7, 19] or the spacetime second member(or the so-called "gradient of the cost function"), $m_U(\mathbf{X}, t)$. The latter option is chosen in this paper, because of its efficiency and lower computational cost [4].

The space time field $m_U(\mathbf{X}, t)$ is decomposed as a sum of separated terms, products of spatial and temporal modes, whose truncation provides a low-rank spacetime approximation. Benefiting from the orthogonalization of the temporal modes, they are directly used as a temporal basis in the spacetime SC formulation, to compute each incremental correction to the displacement field at each iteration of the Gauss-Newton minimization scheme. An energetic criterion is used to select the best low-rank approximation, namely, the number of temporal modes N_p is chosen so that the "power" (*i.e.,* L2 norm) of the reconstruction error is less than a prescribed value ϵ.

3.3 Simulation guided proper-generalized decomposition stereocorrelation (SG-PGD-SC)

Since the choice of a temporal basis is not resticted in PGD-SC, one may benefit from numerical simulation of the hybrid test to guide PGD-SC computations. More precisely, when using the measured force signals synchronized

with image acquisition, one easily gets simulated displacements from the beam model, which covers the region of interest. Then, one may use the best low-rank approximation of the simulated kinematics as temporal shape functions (or a part of it) to initialize PGD-SC computations.

Two strategies may be envisioned:

1. **"Semi SG-PGD-SC".** In the very first PGD-SC iterations, the temporal shape functions are directly imported from the numerical simulation. After reaching pre-convergence of the displacement field, one may switch back to standard PGD-SC to compute the temporal shape functions based on the error estimates.
2. **"Full SG-PGD-SC".** The temporal shape functions are mixed directly by selecting the most "energetic" temporal modes[1] from both the numerical simulations and their error estimates. One should equally note that the set of temporal shape functions extracted from the numerical simulations of the beam model and the one extracted from the spacetime second member are not orthogonal by default. Thus compared to the variant of "Semi SG-PGD-SC", a re-orthongonalization of temporal shape functions has to be performed for "Full SG-PGD-SC,", for instance using a Gram-Schmidt algorithm.

Let us emphasize that, from an existing PGD-SC code, the numerical implementation of Simulation-Guided PGD-SC is non-intrusive and only requires very minimal work.

4 Results and discussions

The experimental campaign consisted of three "runs" with increasing severity. The first two were low amplitude, mostly in the linear and elastic regime. The third one, of higher motion amplitude, induced significant damage (*i.e.,* non-linearities), and was therefore a much more critical part of the experiment. This observation motivated the choice of the third run for the SC analyses.

4.1 Stereocalibration

After the stereocalibration step [18], the FE mesh is projected onto each reference image plane. Figure 8 shows that the external edge of the projected mesh matches the highlighted edges drawn on the ROI very well, qualitatively validating the accuracy of the stereo-calibration. Additionally, a small part of FE-mesh close to the clamping (highlighted in cyan) is removed from the following analyses due to shadowing.

[1] The energetic criterion can be used to select the best low rank approximation [7].

4.2 Recorded force data and temporal modes from numerical simulations

For each individual run, the applied boundary conditions are recorded. Special attention is paid to the synchronization between applied displacement and image acquisition. Figure 9 shows the force signals and the commands on both actuators for run #3. These measurements were used to re-evaluate the dynamic response of the virtual substructure at a sampling rate of 1024 Hz, which made it easier to re-synchronize the model with the data recorded by the controller and the high-speed cameras. This choice has been made to be as close as possible to the hybrid testing conditions, even if it results from an *offline* finite element analysis (*i.e.,* pre-computed before the experiment started) could be used as well for *online* applications.

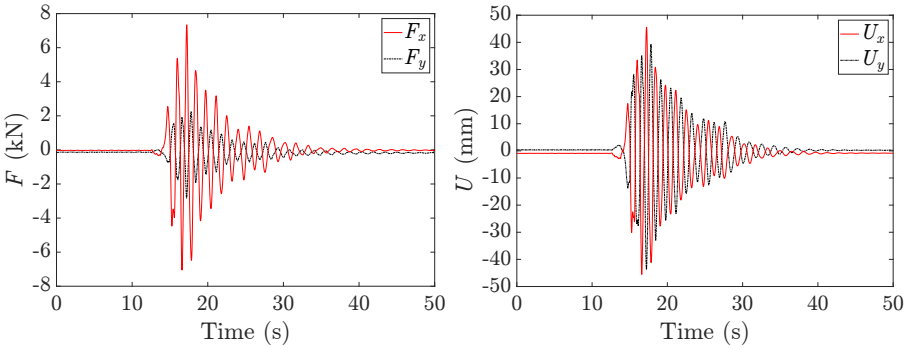

Fig. 9 Recorded boundary conditions for run #3. Forces (left) and displacements (right) prescribed by the actuators.

A standard POD procedure is then performed to obtain the best low-rank approximation of the simulated kinematics at run #3. Figure 10 plots each POD mode ranked by its singular value in descending order. It is observed that the first three POD modes account for more than 99% of the total signal energy.

Since the problem was solved using the HROM discussed in subsubsection 2.1.4, the corresponding spatial modes are shown in Figure 4. They all mainly activate bending and torsional mechanisms at the floor level, as expected from the kinematics of the RCC specimen.

4.3 Performance Comparison

The exact same mesh and convergence criteria are used for the different SC schemes to allow for a fair comparison. For the sake of simplicity, in the following, the frame number t^* is used to represent time (the actual time in seconds is obtained by a mere division by 125).

The global gray-level residual is plotted against the iteration number in Figure 11 to evaluate the convergence speed.

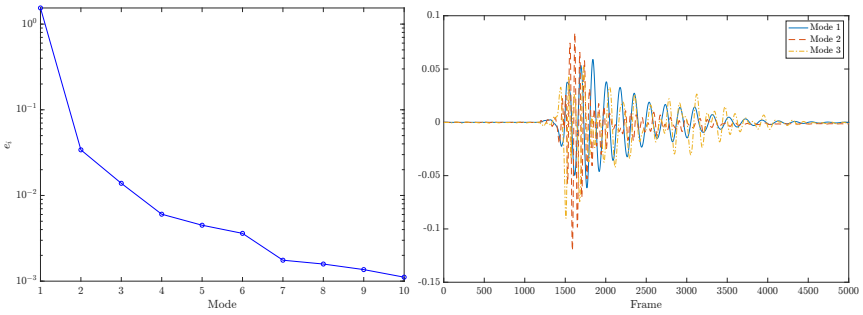

Fig. 10 (left) Singular value of each POD mode for the simulated kinematics. The first three modes concentrate 99% of the total signal energy. (right) First three temporal modes from the simulated kinematics.

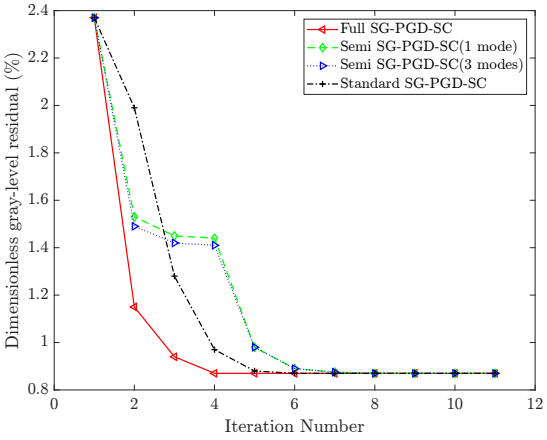

Fig. 11 Dimensionless gray level residuals vs. iteration number. Standard PGD-SC is plotted in black, Semi SG-PGD-SC with one and three modes from simulations are plotted respectively in green and blue, and Full SG-PGD-SC scheme with one simulation mode and 3 POD modes is plotted in red.

Several remarks are worth being made:

1. Semi SG-PGD-SC runs with 1 and 3 simulations modes have a similar convergence speed (having a very sharp decrease at iteration 1 and reaches a plateau between iterations 2 and 4, and after iteration 4, using the temporal modes computed from the gradient of the SC cost-function, the residual decreases quickly to convergence (converged at iteration 11).

   This observation is consistent with the simulation where the first POD mode accounts for more than 98% of the total energy, thus adding additional temporal shape functions has minimal effect in improving the convergence speed. After iteration 4, additional modes are added from the gradient of the spacetime cost-function, leading to a further decrease of gray-level residuals. This effect is seen as the proof of mobilized severe non-linear phenomena that the current numerical model failed to represent.

2. Full SG-PGD-SC exhibits the fastest convergence speed among all PGD-SC versions (*i.e.,* it converged at the 7-th iteration), using one temporal mode from the numerical simulation, and three temporal modes from the gradient of the SC cost-function.
3. All PGD-SC versions reached the same level of gray-level residuals at convergence ($\rho = 0.87\%$). These different schemes also converge to the same results (*i.e.,* the root mean square nodal-displacement differences between all discussed schemes is at the level of displacement uncertainties reported in Table 7), thereby cross-validating the results.
4. The total CPU times[2] for these various schemes are shown in Table 1. The full SG-PGD-SC has the lowest computation time[3] (improved by about 20% as compared to standard PGD-SC) since it needs less iterations to converge (Figure 11). In contrast, the performances of semi SG-PGD-SC and standard PGD-SC are almost identical. Since the numerical simulations of the full test, including the beam, can be performed before the SC computations, the additional numerical cost to import temporal shape functions is negligible.

Table 1 Total CPU times for the different schemes.

Scheme	Average CPU Time (s)
Standard PGD-SC	457
Semi SG-PGD-SC (1 mode)	415
Semi SG-PGD-SC (3 modes)	409
Full SG-PGD-SC	372

4.4 Gray-level residuals

4.4.1 Global gray-level residuals

Figure 12 displays the global gray-level residuals versus frame number. It is observed that at the initial (static) loading stage, the gray-level residual is almost at a (very low) constant level ($\rho = 0.6\%$). During seismic loading, the global gray-level residual reaches its highest levels at frames 1500, 1583, and 1655. After inspecting the corresponding residual frames (Figure 13), these frames correspond to the instants where most opened surface cracks are observed. After the loading has stopped, the gray-level residual gradually returns to a stable level ($\rho = 0.9\%$), which is slightly higher than the initial residual. This observation points to the presence of surface pattern degradation and closed cracks in the RCC specimen.

[2]Loading the image sequence and assembling the spatial Hessian matrix costs some notable time. However, since this preparation stage is equivalent for all versions, only the cost of Gauss-Newton iterations is compared.

[3]The calculations were carried out using a workstation with 48 CPU cores (Intel Platinum 8475B 48C/96T 2.7G) and 512GB of RAM.

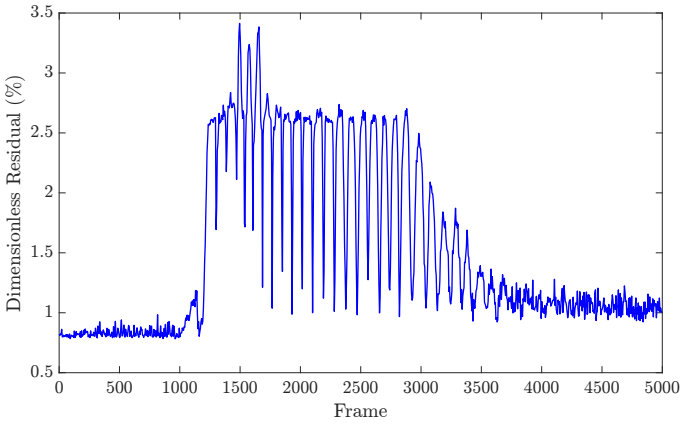

Fig. 12 Global gray-level residual plotted versus frame number (time).

4.4.2 Gray-level residual fields

At the displacement magnitude peak (frame #1655), the camera-wise gray-level residual field $\rho_i(\mathbf{X}, t)$, $i = 1, 2$ and the root mean square (RMS) gray-level residual are displayed in Figure 13. The camera-wise residuals from both cameras clearly reveal the presence of several cracks in the ROI. Because of perspective differences, the two cameras show different sensitivities to cracks, some more "visible" than others. Thus, the residuals cannot simply be used as a *quantitative* indicator but rather a qualitative one. For surface crack detection in SC, setting a somewhat different position and orientation for each camera is highly recommended to provide a least-biased detection.

4.5 Damage Quantification

The necessary linear interpolation[4] of gray levels at each evaluation point involves some approximations and, in turn, contributes to the global gray-level residuals. Assuming that the contributions from cracks in the gray-level residuals are very localized in space and time while the interpolation errors are much more distributed, it is proposed to isolate crack (singular) contributions to the residuals by introducing a reduced observation window containing one of the major cracks that initiated and propagated inside the ROI, as highlighted in Figure 14.

Both the camera-wise GL residual and the global GL residual are re-computed within the cropped region. Figure 15 shows that the changes of re-computed camera-wise GL residuals from both camera and global residual are consistent, thereby implying that the major contribution to the residual is due to the crack contribution rather than interpolation errors.

[4]The high-order interpolant did provide a better accuracy but at a cost of longer computational time. The linear interpolant was selected as a compromise between accuracy and speed to handle the 5,000 image stacks

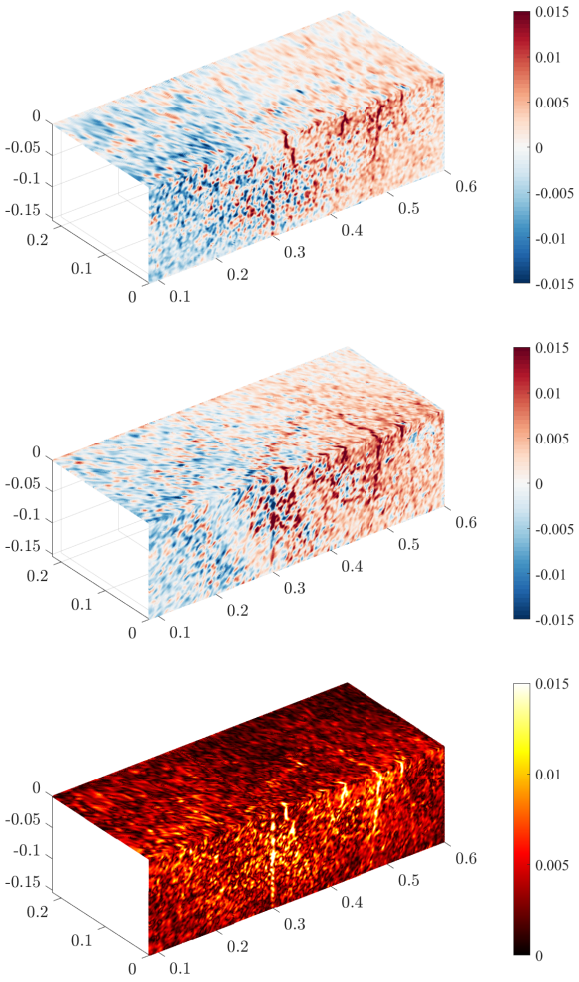

Fig. 13 Gray-level residual fields for frame 1655. (top) Camera 1; (middle) Camera 2; (bottom) RMS of both fields

Focusing on a small time interval about the highest peak (centered at frame 1500, Figure 15), five different frames at $t = 1480, 1490, 1500, 1510, 1520$ were selected (Figure 16). In the first frame, the major crack is not visible. It looks like the crack has reached its full length in the second frame, at time $t = 1490$, indicating that crack initiation can be localized very precisely in time. In the third frame, the crack appears at its apparent full length and largest opening, both contributing to the residual reaching its maximum value. The latter decreases in the fourth and fifth frames, but a faint mark is still perceived along the, now closing, crack. Those observations highlight the sensitivity of the residuals of such an analysis despite their qualitative character.

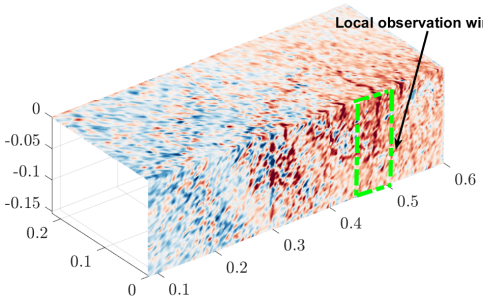

Fig. 14 Reduced observation window highlighted in green to re-compute camera-wise and global gray-level residuals.

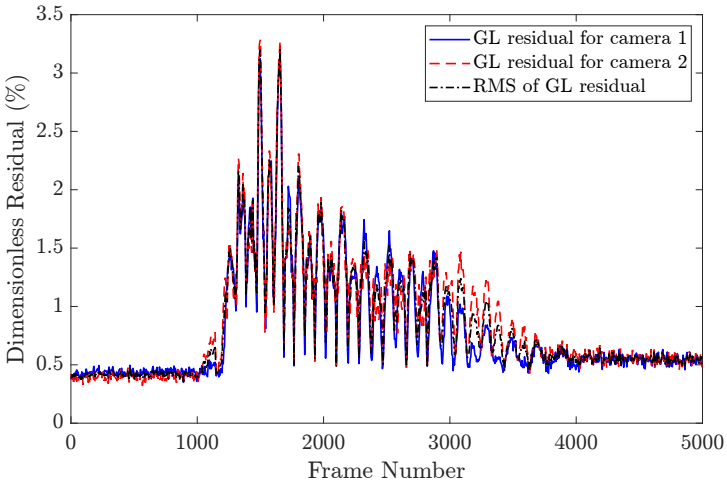

Fig. 15 History of camera-wise and global GL residuals from the reduced observation window

4.6 Comparison between measured and simulated displacement data

After collecting the spacetime displacement data from SG-PGD-SC measurements, it is extremely appealing to compare the temporal modes locally identified from the test to their counterparts extracted from the dynamics of the building (*i.e.,* partly *simulated*, and partly *tested*), which were built using POD to truncate the displacements provided by the model (Figure 10).

When handling *simulated* displacement data with POD, the previous observation suggests that a single temporal mode is dominant. However, the spacetime (POD) decomposition of the *measured* kinematic fields leads to a slightly different conclusion. By plotting the eigenvalues (ranked in descending order), and the first few temporal and spatial modes in Figure 17 and Figure 18, it is concluded that based on the spectrum presented in Figure 17, at least the

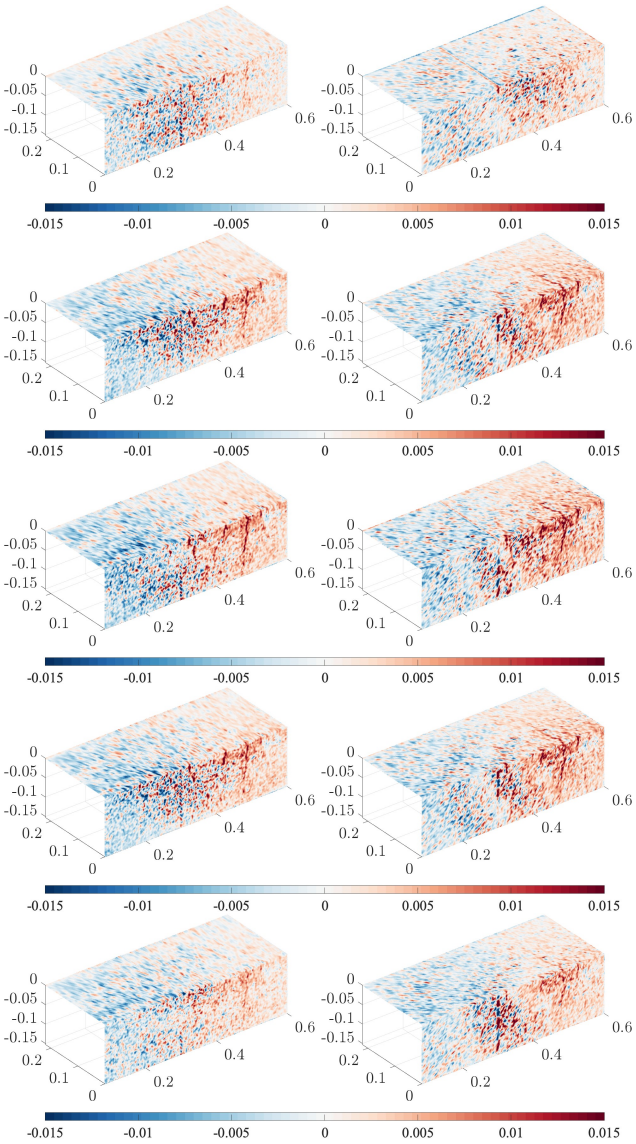

Fig. 16 Snap-shots of camera-wise GL residuals (frames 1480, 1490, 1500, 1510 and 1520 from top to bottom). (left) Camera 1. (right) Camera 2.

first three modes are required to construct the measured displacement field within a minimal error (*i.e.,* less than 2%).

Among these first three POD modes, the first and third spatial modes (Figure 18) appear to involve mostly bending of the concrete beam, in two (very) different directions (as a consequence of the orthogonality of these modes), whereas the second one is more difficult to interpret, although its power is significant.

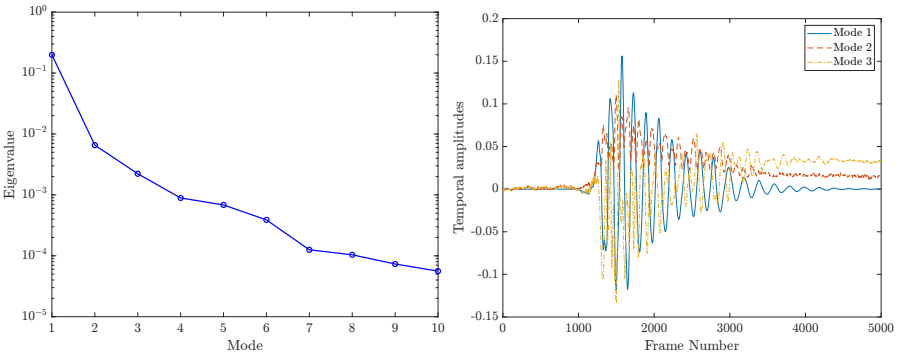

Fig. 17 POD modes extracted from the measured displacements. (left) Eigenvalue against POD modes. (right) First three temporal modes accounting for the majority of power.

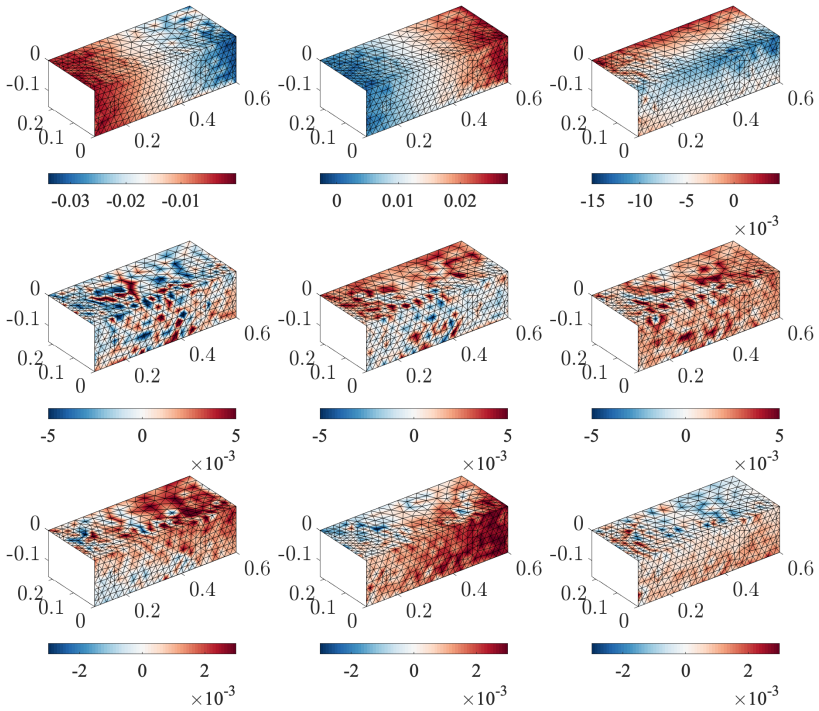

Fig. 18 First three spatial modes of the measured displacements. For each spatial mode, its components along X, Y, Z directions are plotted from left to right. (top) Mode 1, (middle) Mode 2, (bottom) Mode 3.

As a preliminary cross-validation, Figure 19 compares the first POD mode extracted from the measured data to the first temporal mode extracted from the model. These two modes almost overlap at the beginning of the test, showing a good agreement between them. However, a slow drift is also noted

between the two signals for later times, which results from the nonlinear behavior of the tested specimen that the numerical model fails to describe.

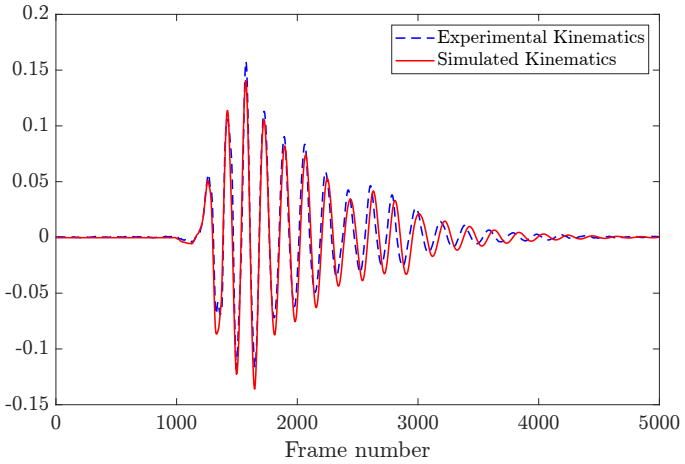

Fig. 19 Comparison of the first POD temporal mode extracted from the measured (blue) and simulated (red) kinematics.

The second (temporal) mode is compared to the global gray-level residual in Figure 20. These two signals exhibit a strong correlation, showing that the second mode associated with the measured displacements is related to local crack-opening and closing. Let us note that these crack-related kinematic nonlinearities are neither available from local displacement sensors, nor easily predictable from numerical models. Using global kinematic data such as SG-PDG-SC to monitor hybrid tests seems to be a promising tool to evaluate these nonlinearities, but also propagate them to the simulated parts of the building using a model updating procedure to better discribe the real-world conditions.

4.7 Comparison with finite element analyses

If hybrid testing allows structural components to be subjected to earthquake conditions, its benefits may be questioned as differences still remain between the specimen and the model. SC is consequently useful for the investigated case as it may be used to quantify the ability of nonlinear multifiber beams (Figure 2) in predicting damage and opening-closure of cracks.

The RCC is simulated *as tested* using the displacements recorded at the top of the specimen at runs #1, #2, and #3. The model includes sixteen multifiber beams, whose cross-sections are discretized into 6×10 surface elements. The threaded rods and longitudinal steel reinforcements are explicitly modeled by adding from four to eight steel fibers to the cross-sections (Figure 21).

The mesh is more refined at the clamp (*i.e.,* where the ROI is located). At the column base, a 5 cm long element first models the connection of the

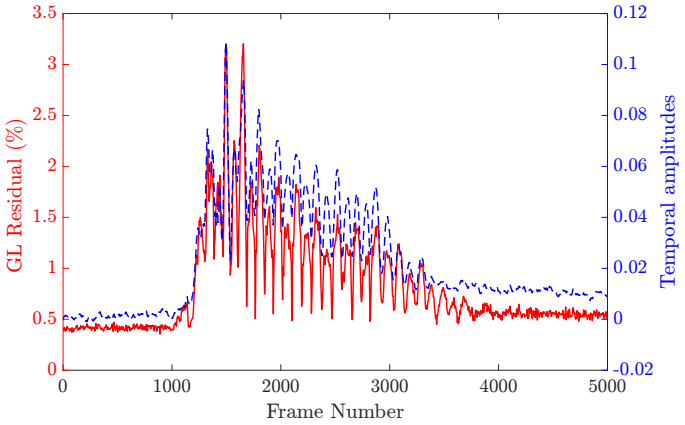

Fig. 20 Comparison between the global gray-level residual (red) and the second temporal mode (blue).

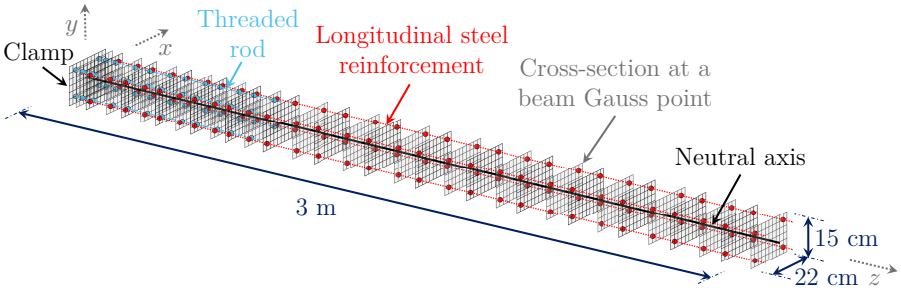

Fig. 21 Multi-fiber mesh of the RCC specimen. Discretized concrete cross-sections on which steel fibers are located.

threaded rods to the reaction wall. Five 15 cm long elements are then distributed over a 75 cm length on which the forces are transmitted from the longitudinal reinforcements to the threaded rods. The remaining length of the beam is finally discretized into ten 22 cm long elements. To be sure that the model is representative of the RCC specimen, the concrete is modeled using the mean properties reported in Table 2. Rotational stiffnesses are also added at column base to account for clamping imperfections. Using the data of Table 3, equivalent stiffnesses $K_{\mathrm{r},xx} = 1,200$ kN $\cdot$ m and $K_{\mathrm{r},yy} = 3,800$ kN $\cdot$ m were identified about the x and y axes, respectively.

Figure 22 compares the numerical and experimental force-displacement responses along the x-axis for runs #1 to #3. It also shows the damage index distribution around the clamp at frame #1480, over a 65 cm length on which degrading mechanisms are expected to be highest. If the force-displacement response agrees with the data recorded on the setup, damage indices are overestimated as cross-sections are already fully damaged at frame #1480, which is not the case on the specimen as only mesocracks are captured by SC. To model stiffness recoveries when opened cracks are closing, the concrete constitutive

law uses an internal crack closure variable η, which quantifies the opening of cracks under cyclic loads [22]. It varies between zero when the cracks are completely closed, and one when they fully open.

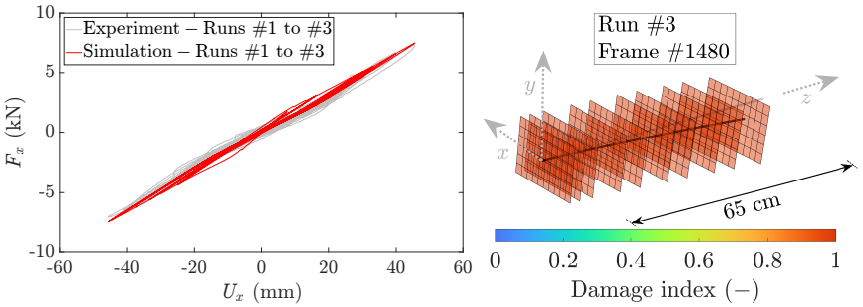

Fig. 22 Results of the finite element analysis. (left) Experimental and predicted force-displacement response. (right) Damage index distribution on the cross-sections of the model for the column base on 30 times amplified deformed mesh (frame #1480).

Figure 23 shows the distribution of index η over the cross-sections close to the clamp at frames #1480, #1490, #1500, #1510, and #1520. The axial strains identified on concrete are also displayed with displacements amplified 35 times to be visible on the deformed mesh. The results show that cracks progressively open from frame #1480 to #1500, which is consistent with Figure 16 as η is equal to one at the areas where the residuals are the highest. From frame #1500 to #1520, η then decreases as the loading direction reverses. The model is able to simulate crack opening, but remains limited as it cannot precisely locate the most damaged areas. Because a transmission length between the threaded rods and the reinforcements doubles the steel ratio from 5 cm to 80 cm, the stiffness of the cross-sections locally increases, so do the axial strains and crack openings reach their extrema at the column base (Figure 23), where only the threaded rods contribute to the strength of the specimen. These results differ from SC observations as the experiment highlighted significant cracking activity from 20 cm to 60 cm from the reaction wall (Figure 16). These local cracks may be explained by the presence of transverse steel reinforcements (*i.e.,* stirrups) that are not explicitly modeled in the multifiber mesh.

The differences between simulation and experiment demonstrate that despite knowing well the material properties, reinforcements, and boundary conditions, local damage (*i.e.,* mesocracking) remains difficult to predict on reinforced concrete structures as damage growth highly depends on the presence of initial defects or discontinuities that cannot be easily observed. SC provides additional data that can be used to complete the results of coarse simulations (as is the case here), or to calibrate refined models.

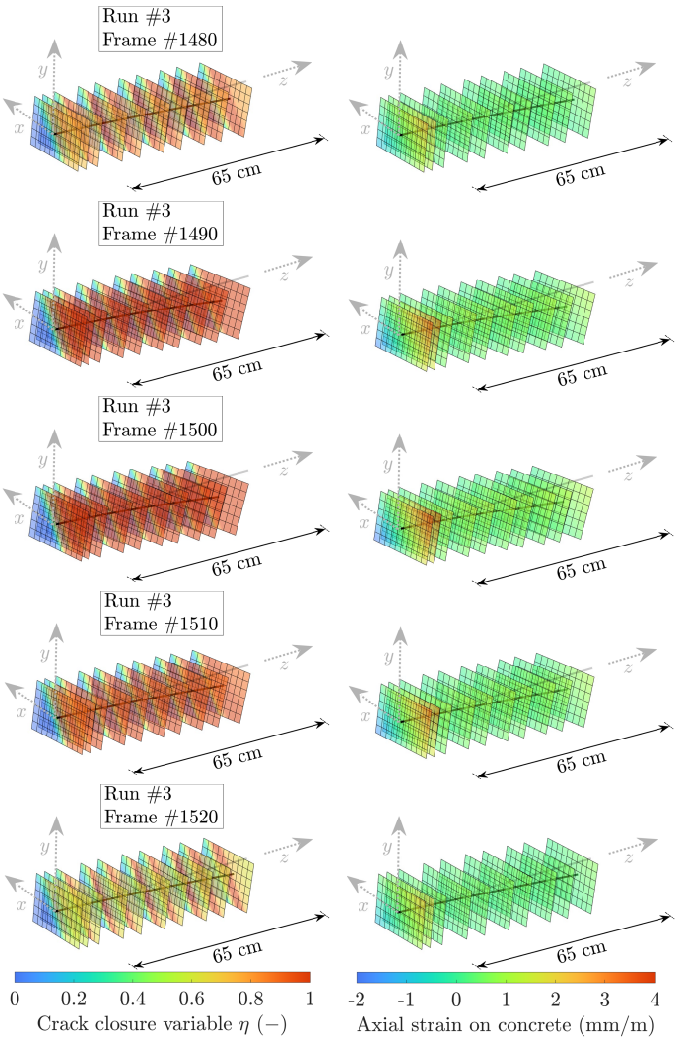

Fig. 23 Deformed mesh amplified 30 times over a 65 cm length from the clamp at frames #1480, #1490, #1500, #1510, and #1520. (left) Crack closure variable distribution. (right) Axial strains in concrete.

5 Conclusion

When handling long time-series of images using spacetime SC, the choice of temporal shape functions is unrestricted. Benefiting from the finite-element representation of SC, Simulation-Guided PGD-SC offers a natural way to construct orthonormal temporal bases in the most flexible manner:
– on the one hand, an important part of the temporal shape functions may come directly from numerical simulations of the experiment itself, providing a "mechanics-educated" initial guess to the problem;
– on the other hand, the remaining temporal shape functions are constructed

on the fly based on the error estimates (gradient of the SC cost function), thereby allowing one to account for nonlinearities or defects that the numerical model fails to account for.

An RCC specimen subjected to a real-time hybrid test was chosen as a validation benchmark, where the (physical) beam itself was one of the most vulnerable substructures of an otherwise virtual three-story building. The force signals were carefully synchronized with image acquisition. It was shown that when using such a mixed approach to construct the temporal basis (*i.e.,* combining both simulation and error estimates), SG-PGD-SC significantly outperformed the classical PGD-SC regarding convergence speed while preserving the measurement accuracy and robustness.

It was also shown that the SC analysis nicely complemented the hybrid test, allowing, for instance, for a direct comparison of global temporal or spatial modes with the computed ones, thereby validating the overall framework but also shedding light onto small differences such as the small drift of the first temporal mode, or highlighting the development of nonlinearities (*i.e.,* damage, plasticity), which are more difficult to capture precisely in the model. Last, focusing on specific features interpreted as cracks in the residuals, their detailed location, growth, opening, and closure were assessed, complementing the more global modal characterization. Overall, the proposed simulation-guided framework opens easier access for handling complex experimental tests. More importantly, it allows for a more discriminative dialog and cross-validation between numerical simulation and actual tests.

Last, let us emphasize that within a full simulation-guided PGD-SC framework, the average CPU time per frame is about 0.07s despite using an FE mesh containing 356,160 evaluation points. This CPU time can be lowered to milliseconds if a coarse mesh with fewer evaluation points is used. This breakthrough opens up a potential avenue for using SG-PGD-SC to monitor the entire hybrid test instead of displacement sensors, or identify constitutive laws to replace specimens or parts of them (*e.g.,* bridge piers) by adaptive numerical models that best fit the data measured by SC. Online model updating allows the complexity of hybrid setups to be reduced, but also improves the representativity of simulated components. If neural networks or optimization methods based on point force-displacement responses are already under study [60–63], SC-based methods could be used instead as they provide many data about damage growth, boundaries, and strains [21, 64, 65]. Extending SC-based model updating to hybrid testing would require using simulation-guided PGD-SC with careful C++ and GPU implementations to process image stacks *online*, which is already possible for pseudo-dynamic experiments.

Acknowledgements

The authors would like to thank several members of the Laboratory of Mechanics Paris-Saclay, namely Olivier Rateau, Laeticia Szturycz, Rémi Legroux, and Xavier Fayolle for their technical support. JG and FH acknowledge the support

of the International Research Training Group on Computational Mechanics Techniques in High Dimensions GRK 2657 funded by the German Research Foundation (DFG) under Grant Number 433082294.

References

[1] Helfrick, M.N., Niezrecki, C., Avitabile, P., Schmidt, T.: 3D digital image correlation methods for full-field vibration measurement. Mechanical Systems and Signal Processing **25**(3), 917–927 (2011). https://doi.org/10.1016/j.ymssp.2010.08.013

[2] Hild, F., Roux, S.: Digital image correlation. In: Rastogi, P., Hack, E. (eds.) Optical Methods for Solid Mechanics. A Full-Field Approach, pp. 183–228. Wiley-VCH, Weinheim (Germany) (2012)

[3] Le Gourriérec, C., Chang, X., Durand, B., Roux, S.: High speed stereo-vision study of laminated glass fragmentation upon impact. Glass Structure and Engineering (2023). https://doi.org/10.1007/s40940-023-00231-2

[4] Chang, X., Le Gourriérec, C., Hild, F., Roux, S.: Brightness and contrast corrections for stereocorrelation: Global and instantaneous formulation with spatial regularization. Mechanical Systems and Signal Processing **208**, 111057 (2024). https://doi.org/10.1016/j.ymssp.2023.111057

[5] Chang, X., Le Gourriérec, C., Hild, F., Roux, S.: Brightness and contrast corrections for space–time stereocorrelation via proper generalized decomposition. Mechanical Systems and Signal Processing **224**, 111946 (2025). https://doi.org/10.1016/j.ymssp.2024.111946

[6] Passieux, J.-C., Bouclier, R., Périé, J.N.: A Space-Time PGD-DIC Algorithm:. Experimental Mechanics **58**(7), 1195–1206 (2018). https://doi.org/10.1007/s11340-018-0387-2

[7] Chang, X., Le Gourriérec, C., Turpin, L., Berny, M., Hild, F., Roux, S.: Proper generalized decomposition stereocorrelation to measure kinematic fields for high speed impact on laminated glass. Computer Methods in Applied Mechanics and Engineering **415**, 116217 (2023). https://doi.org/10.1016/j.cma.2023.116217

[8] Luo, P.F., Chao, Y.J., Sutton, M.A., Peters, W.H.: Accurate measurement of three-dimensional deformations in deformable and rigid bodies using computer vision. Experimental Mechanics **33**(2), 123–132 (1993). https://doi.org/10.1007/BF02322488

[9] Sutton, M.A., Orteu, J.J., Schreier, H.: Image Correlation for Shape, Motion and Deformation Measurements: Basic Concepts, Theory and

Applications. Springer, New York, NY (USA) (2009)

[10] Seitz, S.M., Curless, B., Diebel, J., Scharstein, D., Szeliski, R.: A comparison and evaluation of multi-view stereo reconstruction algorithms. In: 2006 IEEE Computer Society Conference on Computer Vision and Pattern Recognition (CVPR'06), vol. 1, pp. 519–528 (2006). https://doi.org/10.1109/CVPR.2006.19

[11] Vu, H.-H., Labatut, P., Pons, J.-P., Keriven, R.: High accuracy and visibility-consistent dense multiview stereo. IEEE Transactions on Pattern Analysis and Machine Intelligence **34**(5), 889–901 (2012). https://doi.org/10.1109/TPAMI.2011.172

[12] Dubreuil, L., Dufour, J.-E., Quinsat, Y., Hild, F.: Mesh-based shape measurements with stereocorrelation. Exp. Mech. **56**(7), 1231–1242 (2016)

[13] Pierré, J.-E., Passieux, J.-C., Périé, J.-N.: Finite Element Stereo Digital Image Correlation: Framework and Mechanical Regularization. Experimental Mechanics **57**(3), 443–456 (2017)

[14] Beaubier, B., Dufour, J.E., Hild, F., Roux, S., Lavernhe-Taillard, S., Lavernhe-Taillard, K.: CAD-based calibration of a 3D-DIC system: Principle and application on test and industrial parts. Exp. Mech. **54**(3), 329–341 (2014)

[15] Dufour, J.-E., Hild, F., Roux, S.: Shape, Displacement and Mechanical Properties from Isogeometric Multiview Stereocorrelation. J. Strain Analysis **50**(7), 470–487 (2015)

[16] Wang, Y., Charbal, A., Dufour, J.-E., Hild, F., Roux, S., Vincent, L.: Hybrid multiview correlation for measuring and monitoring thermomechanical fatigue test. Exp. Mech. **56**(DOI: 10.1007/s11340-019-00500-8), 845–860 (2019)

[17] Hild, F., Roux, S.: Displacement uncertainties with multiview correlation schemes. Journal of Strain Analysis for Engineering Design **55**(7-8), 199–211 (2020). https://doi.org/10.1177/0309324720927102

[18] Berny, M., Archer, T., Beauchêne, P., Mavel, A., Hild, F.: Displacement Uncertainty Quantifications in T3-Stereocorrelation. Experimental Mechanics **61**, 771–790 (2021)

[19] Berny, M., Jailin, C., Bouterf, A., Hild, F., Roux, S.: Mode-enhanced space-time dic: applications to ultra-high-speed imaging. Measurement Science and Technology **29**(12), 125008 (2018)

[20] Nakashima, M., Kato, H., Takaoka, E.: Development of real-time pseudo

dynamic testing. Earthquake Engineering and Structural Dynamics **21**(1), 79–92 (1992). https://doi.org/10.1002/eqe.4290210106

[21] Neggers, J., Mathieu, F., Hild, F., Roux, S., Swiergiel, N.: Improving full-field identification using progressive model enrichments. International Journal of Solids and Structures **118-119**, 213–223 (2017). https://doi.org/10.1016/j.ijsolstr.2017.03.013

[22] Richard, B., Ragueneau, F.: Continuum damage mechanics based model for quasi-brittle materials subjected to cyclic loadings: Formulations, numerical implementation and applications. Engineering Fracture Mechanics **98**, 383–406 (2013). https://doi.org/10.1016/j.engfracmech.2012.11.013

[23] Chaturantabut, S., Sorensen, D.C.: Nonlinear model reduction via discrete empirical interpolation. Society for Industrial and Applied Mathematics **32**(5) (2010). https://doi.org/10.1137/090766498

[24] Tiso, P., Rixen, D.J.: Discrete empirical interpolation method for finite element structural dynamics. Topics in Nonlinear Dynamics, Volume 1, 203–212 (2013). https://doi.org/10.1007/978-1-4614-6570-6_18

[25] Farhat, C., Avery, P., Chapman, T., Cortial, J.: Dimensional reduction of nonlinear finite element dynamic models with finite rotations and energy-based mesh sampling and weighting for computational efficiency. International Journal for Numerical Methods in Engineering **98**(1), 625–662 (2014). https://doi.org/10.1002/nme.4668

[26] Farhat, C., Chapman, T., Avery, P.: Structure-preserving, stability, and accuracy properties of the energy-conserving sampling and weighting method for the hyper reduction of nonlinear finite element dynamic models. International Journal for Numerical Methods in Engineering **102**(5), 1077–1110 (2015). https://doi.org/10.1002/nme.4820

[27] Bodnar, B., Larbi, W., Titirla, M., Deü, J.-F., Gatuingt, F., Ragueneau, F.: Comparison of pod-udeim and pod-ecsw model order reduction in the case of damaging rc structures subjected to earthquakes. Proceedings of the 9th ECCOMAS Thematic Conference on Computational Methods in Structural Dynamics and Earthquake Engineering, Athens, Greece, 4492–4510 (2023). https://doi.org/10.7712/120123.10736.21260

[28] Bodnar, B., Larbi, W., Titirla, M., Deü, J.-F., Gatuingt, F., Ragueneau, F.: Hyper-reduced order models for accelerating parametric analyses on reinforced concrete structures subjected to earthquakes. Computer-Aided Civil and Infrastructure Engineering **39**(4), 476–497 (2024) https://arxiv.org/abs/https://onlinelibrary.wiley.com/doi/pdf/10.1111/mice.13120. https://doi.org/10.1111/mice.13120

[29] Souid, A., Delaplace, A., Ragueneau, F., Desmorat, R.: Pseudo-dynamic testing and nonlinear substructuring of damaging structures under earthquake loading. Engineering Structures **31**(5), 1102–1110 (2009). https://doi.org/10.1016/j.engstruct.2009.01.007

[30] Han, Q., Zhao, Y., Lu, Y., Wang, S.: Substructured hybrid test examining the seismic response of point-supported glass façades attached to large-span spatial steel structures. Engineering Structures **266**(114545) (2022). https://doi.org/10.1016/j.engstruct.2022.114545

[31] Hakuno, M., Shidawara, M., Hara, T.: Dynamic destructive test of a cantilever beam controlled by an analog-computer. Transactions of the Japan Society of Civil Engineers **1969**(171), 1–9 (1969). https://doi.org/10.2208/jscej1969.1969.171_1

[32] Takanashi, K., Udagawa, K., Seki, M., Okada, T., Tanaka, H.: Non-linear earthquake response analysis of structures by a computer-actuator on-line system (part 1 detail of the system). Transcript of the Architectural Institute of Japan (No. 229) **229**(190), 77–83 (1975). https://doi.org/10.3130/aijsaxx.229.0_77

[33] Balendra, T., Lam, K.-Y., Liaw, C.-Y., Lee, S.-L.: Behavior of eccentrically braced frame by pseudo-dynamic test. Journal of Structural Engineering **113**(4), 673–688 (1987). https://doi.org/10.1061/(ASCE)0733-9445(1987)113:4(673)

[34] Molina, F.J., Verzeletti, G., Magonette, G., Buchet, P., Géradin, M.: Bi-directional pseudodynamic test of a full-size three-storey building. Earthquake Engineering and Structural Dynamics **28**(12), 1541–1566 (1999). https://doi.org/10.1002/(SICI)1096-9845(199912)28:12⟨1541::AID-EQE880⟩3.0.CO;2-R

[35] Dermitzakis, S.N., Mahin, S.A.: Development of substructuring techniques for on-line computer controlled seismic performance testing. Report UCB/EERC - 85/04, Earthquake Engineering Research Center, University of California, Berkeley (1987)

[36] Nakashima, M., Kaminoso, T., Ishida, M., Ando, K.: Integration techniques for substructuring pseudodynamic test. Journal of Structural and Construction Engineering (Transactions of AIJ) **417**, 107–117 (1990). https://doi.org/10.3130/aijsx.417.0_107

[37] Jennings, E., van de Lindt, J.W., Ziaei, E., Mochizuki, G., Pang, W., Shao, X.: Retrofit of a soft-story woodframe building using sma devices with full-scale hybrid test verification. Engineering Structures **80**, 469–485 (2014). https://doi.org/10.1016/j.engstruct.2014.09.021

[38] Abbiati, G., Bursi, O.S., Caperan, P., Di Sarno, L., Molina, F.J., Paolacci, F., Pegon, P.: Hybrid simulation of a multi-span rc viaduct with plain bars an sliding bearings. Earthquake Engineering and Structural Dynamics **44**(13), 2221–2240 (2015). https://doi.org/10.1002/eqe.2580

[39] Kallioras, S., Pohoryles, D.A., Bournas, D., Molina, F.J., Pegon, P.: Seismic performance of a full-scale five-story masonry-infilled rc building subjected to substructured pseudodynamic tests. Earthquake Engineering and Structural Dynamics **52**(12), 3649–3678 (2023). https://doi.org/10.1002/eqe.3940

[40] Tian, Y., Chen, J., Du, C., Sun, Z., Li, Q., Wang, D., Wang, T.: Experimental study on the seismic performance of a curved bridge via large-scale hybrid tests. Engineering Structures **304**(117699) (2024). https://doi.org/10.1016/j.engstruct.2024.117699

[41] Bodnar, B., Larbi, W., Titirla, M., Deü, J.-F., Gatuingt, F., Ragueneau, F.: Modelling of a PsD hybrid test on a RC column/beam junction combining a multifibre beam model and a POD-ROM approach. Computational Modelling of Concrete and Concrete Structures, Euro-C 2022, 414–423 (2022). https://doi.org/10.1201/9781003316404-49

[42] Iemura, H., Igarashai, A., Takahashi, Y.: Substructured hybrid techniques for actuator loading and shake table tests. First International Conference on Advances in Structural Engineering and Mechanics, Seoul, South Korea (1999)

[43] Igarashi, A., Iemura, H., Suwa, T.: Development of substructured shaking table test method. Proceedings of the 12th World Conference on Earthquake Engineering (2000)

[44] Dong, B., Sause, R., Ricles, J.M.: Accurate real-time hybrid earthquake simulations on large-scale mdof steel structure with nonlinear viscous dampers. Earthquake Engineering and Structural Dynamics **44**(2), 2035–2055 (2015). https://doi.org/10.1002/eqe.2572

[45] Wang, J.-T., Gui, Y., Zhu, F., Jin, F., Zhou, M.-X.: Real-time hybrid simulation of multi-story structures installed with tuned liquid dampers. Structural Control and Health Monitoring **23**(7), 1015–1031 (2016). https://doi.org/10.1002/stc.1822

[46] Luo, L., Jiang, N.: Constrained mode-damping solvent extraction combined method for the soil incorporation into a real-time hybrid test of the soil-structure system. Buildings **12**(9), 1478 (2022). https://doi.org/10.3390/buildings12091468

[47] Guo, W., Wang, Y., Zeng, C., Wang, T., Gu, Q., Zhou, H., Zhou, L.,

Hou, W.: Moving safety evaluation of high-speed train on post-earthquake bridge utilizing real-time hybrid simulation. Journal of Earthquake Engineering **27**(2), 284–313 (2021). https://doi.org/10.1080/13632469.2021.1999869

[48] Zhou, Z., Zhang, D., Zhang, Y., Li, N., Gao, S., Yue, Y.: Real-time hybrid simulation incorporating machine learning for deep-water bridges subjected to seismic ground motion with fluid-structure dynamic interaction. Soil Dynamics and Earthquake Engineering **175**(108263) (2023). https://doi.org/10.1016/j.soildyn.2023.108263

[49] Lin, Y., Xu, Y., Wang, A., Chai, W., Wang, Y., Xu, W., Zong, Z.: Implementation of real-time hybrid simulation using a large shake table with onboard actuators. Engineering Structures **305**(117724) (2024). https://doi.org/10.1016/j.engstruct.2024.117724

[50] Davenne, L., Ragueneau, F., Mazars, J., A., I.: Efficient approaches to finite element analysis in earthquake engineering. Computers and Structures **81**(12), 1223–1239 (2003). https://doi.org/10.1016/S0045-7949(03)00038-5

[51] Strutt, J.W.: The theory of sound, volume 2 (1877). https://doi.org/10.1017/CBO9781139058094

[52] Tao, J., Mercan, O., Calayir, M.: Multi-rate real-time hybrid simulation with adaptive discrete feedforward controller-based compensation strategy. Earthquake Engineering and Structural Dynamics **53**(3), 1260–1284 (2023). https://doi.org/10.1002/eqe.4069

[53] Bodnar, B., Titirla, M., Gatuingt, F., Ragueneau, F., Larbi, W., Ragueneau, F.: Bidirectional real-time hybrid test on a steel column virtually connected to a reinforced concrete substructure. Journal of Physics: Conference Series **2647**(14), 142007 (2024). https://doi.org/10.1088/1742-6596/2647/14/142007

[54] Pegon, P., Pinto, A.V.: Pseudo-dynamic testing with substructuring at the elsa laboratory. Earthquake Engineering and Structural Dynamics **29**(7), 905–925 (2000). https://doi.org/10.1002/1096-9845(200007)29:7⟨905::AID-EQE941⟩3.0.CO;2-P

[55] Loève, M.: Probability theory vol. ii. Graduate Texts in Mathematics **46 (4 ed.)** (1978)

[56] Ayoub, N., Deü, J.-F., Larbi, W., Pais, J., Rouleau, L.: Application of the pod method to nonlinear dynamic analysis of reinforced concrete frame structures subjected to earthquakes. Engineering Structures **270**(114854) (2022). https://doi.org/10.1016/j.engstruct.2022.114854

[57] Leissa, A.W.: The historical bases of the rayleigh and ritz methods. Journal of Sound and Vibration **287**(4-5), 961–978 (2005). https://doi.org/10.1016/j.jsv.2004.12.021

[58] Charbal, A., Roux, S., Hild, F., Vincent, L.: Regularised digital-level corrections for infrared image correlation. Quantitative InfraRed Thermography Journal **15**(2), 172–193 (2018). https://doi.org/10.1080/17686733.2018.1425955

[59] Charbal, A., Dufour, J.-E., Guery, A., Hild, F., Roux, S., Vincent, L., Poncelet, M.: Integrated Digital Image Correlation considering gray level and blur variations: Application to distortion measurements of IR camera. Optics and Lasers in Engineering **78**, 75–85 (2016). https://doi.org/10.1016/j.optlaseng.2015.09.011

[60] Elanwar, H.H., Elnashai, A.S.: Framework for online model updating in earthquake hybrid simulations. Journal of earthquake Engineering **20**(1), 80–100 (2016). https://doi.org/10.1080/13632469.2015.1051637

[61] Ou, G., Dyke, S.J., A., P.: Real time hybrid simulation with online model updating: An analysis of accuracy. Mechanical Systems and Signal Processing **84**(B), 223–240 (2017). https://doi.org/10.1016/j.ymssp.2016.06.015

[62] Al-Subaihawi, S., Ricles, J.M., Quiel, S.E.: Online explicit model updating of nonlinear viscous dampers for real time hybrid simulation. Soil Dynamics and Earthquake Engineering **157**(107108) (2022). https://doi.org/10.1016/j.soildyn.2021.107108

[63] Mokhtari, F., Imanpour, A.: A digital twin-based framework for multi-element seismic hybrid simulation of structures. Mechanical Systems and Signal Processing **186**(109909) (2023). https://doi.org/10.1016/j.ymssp.2022.109909

[64] Vargas, R., Neggers, J., Canto, R.B., Rodrigues, J.A., Hild, F.: Analysis of wedge splitting test on refractory castable via integrated dic. Journal of the European Ceramic Society **36**(16), 4309–4317 (2016). https://doi.org/10.1016/j.jeurceramsoc.2016.07.007

[65] Hamadouche, I., Seyedi, D.M., Hild, F.: Damage detection and quantification via multiview dic at varying scale. Experimental Mechanics **64**, 675–689 (2024). https://doi.org/10.1007/s11340-024-01038-0

[66] Chambreuil, C., Giry, C., Ragueneau, F., P., L.: Identification methods of material-based damping for cracked reinforced concrete beam models. Earthquake Engineering and Structural Dynamics **52**(7), 2156–2178 (2023). https://doi.org/10.1002/eqe.3875

[67] Leclerc, H., Neggers, J., Mathieu, F., Roux, S., Hild, F.: Correli 3.0. Agence pour la Protection des Programmes, Paris (France). IDDN.FR.001.520008.000.S.P.2015.000.31500 (2015)

A Description of the three-story frame structure

A.1 Reinforced concrete column

The specimen is fabricated using a concrete of class C 30/37. Its steel reinforcements are designed to ensure that the 15 × 22 cm cross-section of the 3 m long RCC can withstand at least 10 kN along its strong axis. Four longitudinal reinforcements are positioned at corners to tolerate bending, each having a 16 mm diameter. To also prevent from shear collapse mechanisms (*e.g.,* in particular, at the clamp where the strength of the cross-section is more challenging to predict), twenty-four transverse reinforcements having a diameter of 6 mm are added to the reinforcing cage. They are separated by spacings between 6.5 cm and 15 cm, with a 1 cm thick concrete cover to protect the steel reinforcement.

It is set up horizontally as its self-weight is negligible compared to the transverse loads, but also because the vertical actuator partly supports it to avoid initiating mesocracks in bending before the experiment starts. Quasi-static pretests evaluate the initial stiffnesses along the x and y-axes needed for substructuring (see Table 3).

The RCC is anchored to the reaction wall using four threaded 16 mm in diameter rods. All are drowned in an 80 cm concrete length to ensure that concrete-steel interfaces transfer a maximum bending moment of 30 kN·m from the RCC to the reaction wall. At the column base, a 1 cm thick plate is used as a permanent formwork to set the location of the threaded rods. The rods are then tightened to a 3 cm thick plate equipped with cavities, inside which the nuts settle. The plate is finally fixed to the reaction wall for completing the clamping system.

The RCC specimen is virtually pin-connected at its top to the numerical model (Figure 1). The choice of a pin connection has been made to simplify the physical/virtual boundaries as complete 6-DOF links require controlling multiaxial loading systems (*e.g.,* hexapod), which are not common for hybrid testing [40] and almost impossible to use for RTHTs.

A.2 Steel reinforcements and clamping system of the reinforced concrete column

Table 2 Concrete mechanical properties with confidence intervals of 95 %.

Young's modulus	27.1 ± 4.9 GPa
Compressive strength	35.6 ± 7.9 MPa
Tensile strength	3.3 ± 0.5 MPa

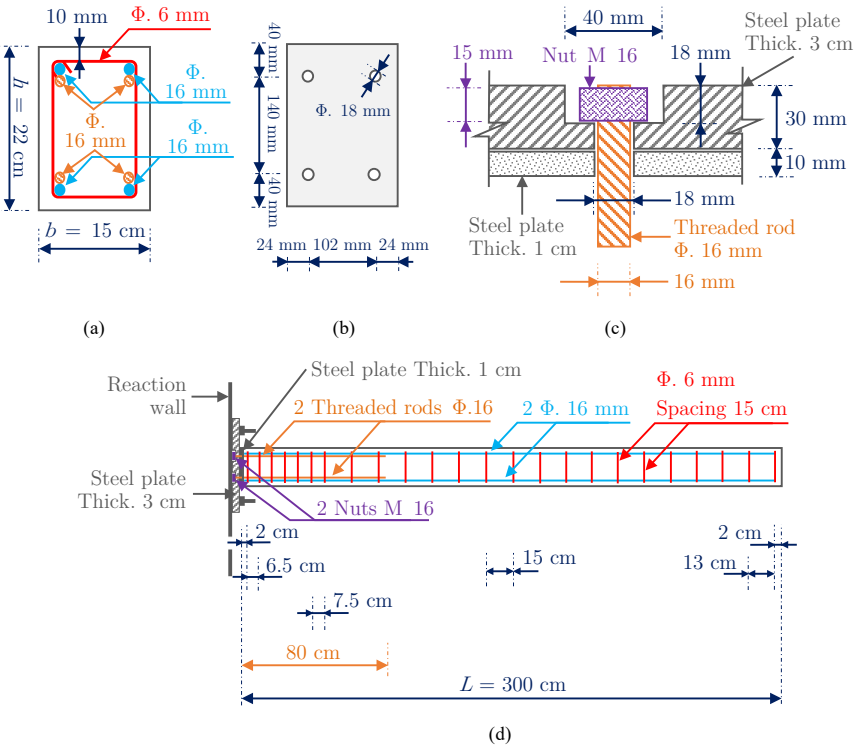

Fig. 24 Cross-section of the reinforced concrete beam at the clamp. (a) 1-cm thick steel plate at the clamp. (b) Focus on a threaded rod connection at the clamp. (c) Longitudinal section of the reinforced concrete beam (d)

Table 3 Initial stiffness components of the RCC specimen.

Transverse stiffness (measured)	K_{xx}	403 kN/m
Transverse stiffness (measured)	K_{yy}	197 kN/m
Axial stiffness (computed)	K_{zz}	347,000 kN/m

A.3 Virtual substructure

The three-story reinforced concrete frame building (Figure 2) is used as a virtual substructure, on which geometrical irregularities in plane and height generate torsion at floor level. All stories are 3 m high, each with spans of 3 m. The columns have a 18 × 18 cm square cross-section, and the beams have a 15 × 30 cm rectangular one. To model floors in a simplified way, longitudinal beams are separated by a center-to-center distance of 1.5 m. Ribbed bars having diameters of 14 mm and 8 mm reinforce the cross-sections along the longitudinal and transverse directions, with a 3 cm thick concrete cover to protect the steel reinforcements.

A mass per unit area of 500 kg/m^2 is proportionally allocated to the nodes that connect transverse and longitudinal beams, then linearly distributed to

account for dead and live loads. Mass densities of 2350 kg/m^3 and 7850 kg/m^3 are used to model concrete and steel, respectively, which results in a structure that weighs 58.8 t. A constant Rayleigh viscous damping is added to the model [51]. It equals 2 % at 1.61 Hz (*i.e.,* eigenfrequency #1) and 5.48 Hz (*i.e.,* eigenfrequency #6) so that its value reaches a minimum around the main eigenmodes [66].

A.4 Mechanical properties of concrete and steel

Table 4 Concrete properties.

Young's modulus	E	36.3 GPa
Poisson's ratio	ν	0.2
Initial energy threshold for damage activation	Y_0	83 J/m^3
Brittleness coefficient	A_d	2.9×10^{-2} m^3/J
Kinematic hardening surface modulus	γ	7.0 GPa
Kinematic hardening pseudo potential modulus	a	7.0×10^{-6} Pa^{-1}
Mean closure stress	σ_f	-3.0 MPa
Compressive strength	f_c	-15.0 MPa
Plastic surface modulus	α_f	0.25
Plastic pseudo potential modulus	α_ϕ	0.91
Plastic hardening modulus	a_R	5.5 GPa
Plastic hardening coefficient	b_R	600
Density	ρ_c	2350 kg/m^3

Table 5 Steel properties.

Young's modulus	E	210 GPa
Poisson's ratio	ν	0.2
Yield stress	f_y	500 MPa
Kinematic hardening surface modulus	C	1 GPa
Density	ρ_s	7850 kg/m^3

B Hardware and Software parameters of the stereovision system

Table 6 Camera and acquisition parameters of the stereovision system

Cameras	Photron® SA-5
Definition	1024×640 pixels
Color filter	none
Gray Levels rendering	8 bits
Lens	Nikon AF Nikkor 24 mm f/2.8D
Aperture	f/11
Field of view	800 mm × 500 mm = 0.4 m^2
Image scale	0.93 mm/px (in the center)
Stereo-angle	left camera: 17°, right camera: 38°
Stand-off distance	left camera: 1.6 m, right camera: 0.9 m
Image acquisition rate	125 fps
Patterning technique	B/W paints
Pattern feature size	From 2 to 16 pixels

Table 7 SC analysis parameters.

DIC software	Correli 3.0 [67]
Image filtering	None
Element size	12–13 mm (or 13–14 px, see Figure 8)
Shape functions	Linear (T3 elements)
Evaluation points (per element)	528 (*i.e.,* $N_{\text{IP}} \approx 23$)
Matching criterion	Sum of squared differences
Interpolant	Linear
Displacement noise-floor	$[\sigma(U_x), \sigma(U_y), \sigma(U_z)] = [6.3, 4.7, 4.9]$ µm